Progress In Electromagnetics Research B, Vol. 50, 273–293, 2013

ALGORITHM FOR PROFILE FUNCTION CALCULATION OF 3D OBJECTS: APPLICATION FOR RADAR TARGET IDENTIFICATION IN LOW FREQUENCY

Yanhua Wen[1, *], Nicole de Beaucoudrey[1], Janic Chauveau[2], and Philippe Pouliguen[3]

[1]IETR UMR CNRS 6164, Université de Nantes, La Chantrerie, rue C. Pauc, Nantes 44306, France

[2]DGA: Direction Générale de l'Armement, DGA Maîtrise de l'Information, BP 7, Rennes Armées 35998, France

[3]DGA DS/MRIS, Bagneux 92221, France

Abstract—Ramp response technique in low frequency can be used for generating 3-dimensional images of radar targets (even stealthy or buried targets) so as to identify them. This technique uses the target profile function, which is defined as its transverse cross-sectional area versus distance along the observing direction. For mutually orthogonal observing views, reconstructed 3D images are quite accurate. However, in practice, due to the bias introduced from the response in shadow region and from limited non-orthogonal observing directions, reconstructions become distorted. To evaluate the quality of the reconstruction and to further identify objects from their reconstruction, we need to calculate profile functions of 3D reconstructed objects in arbitrary directions. Therefore, in this paper, we propose an algorithm meeting this needs.

1. INTRODUCTION

Recently, radar in low frequencies has attracted much attention, because it helps countering the problem that stealthy targets, with adapted shapes or absorbing materials, return a very weak radar signal in usual radar frequency bands [1]. Low frequency radars using UHF (Ultra High Frequency, 300 MHz–3 GHz) and VHF (Very High

Received 21 December 2012, Accepted 9 April 2013, Scheduled 11 April 2013

* Corresponding author: Yanhua Wen (yan-hua.wen@etu.univ-nantes.fr).

Frequency, 30 MHz–300 MHz) as well as HF (High Frequency, 1 MHz–30 MHz) correspond to the Rayleigh region and the resonance region for object dimensions respectively small and of the same order, compared to electromagnetic wavelengths [2–4]. Although low frequency bands cannot provide high resolution, they can give useful information about the target's size and volume which contributes greatly to obtain target's global shape. The use of transient back-scattered response resulting from a wave in the form of ramp function was first applied to radar targets identification by Kennaugh and Moffatt in 1965 [5]. Such a ramp response was found to be approximately proportional to the profile function of the radar target, which is defined as its transverse cross-sectional area versus distance along the line-of-sight parallel to the incident wave direction. This property was applied to reconstruct radar targets' shape by Young [6, 7]. His method, well known as the ramp response technique, uses the profile functions from only 3 mutually orthogonal viewing angles and encloses the unknown target with approximate limiting surfaces to generate likely contours, then iteratively fits some geometrical parameters to obtain optimal images. After that, considerable efforts have been made for ramp response technique using Young's algorithm, with application to electromagnetic scattering [8–14] as well as acoustic imaging of underwater objects [15, 16]. However, Young's algorithm is limited to single convex objects while a more recent algorithm [17] overcomes this limitation. Another class of methods consists to apply algorithms of reconstruction from projections, but they require a considerable number of viewing angles and plane-symmetrical objects [18–20].

To evaluate the quality of the reconstruction and to further automatically identify objects from their reconstruction, we need to compare initial profile functions to profile functions of reconstructed objects. Consequently, in this paper, we present an algorithm for calculating profile functions from 3D objects in arbitrary directions. Then, we apply this algorithm to quantitatively evaluate the quality of image reconstructions, using errors between observed profile functions of initial objects and calculated profile functions of reconstructed objects. Moreover, we apply this algorithm to further identify radar targets from their reconstructed images, with calculated profile functions in arbitrary directions and a database of possible models for targets.

This paper is organized as follows: Firstly, in Section 2, the ramp response, the profile function and the algorithm of 3D image reconstruction from profile functions are presented. Then, in Section 3, the algorithm for calculating geometrical profile functions from a 3D object is introduced and algorithm verification is described. Finally,

in Section 4, two applications of this algorithm, namely the quality evaluation of image reconstructions and the further identification from their reconstructed images, are presented.

2. 3D IMAGE RECONSTRUCTION FROM RAMP RESPONSE

In this section, we briefly recall the ramp response, the profile function and the 3D image reconstruction [5, 6, 17].

2.1. Ramp Response

The ramp response of a radar target, $h_r(t)$, is defined as the far field back-scattered wave resulting from illumination by a plane electromagnetic wave with a temporal ramp waveform. In time domain, it is the second integral of its impulse response, $h_i(t)$, and it can also be expressed as the Inverse Fourier Transform (IFT) of the weighted transfer function, $H_r(j\omega)$, with $\omega = 2\pi f$ the angular frequency and $H(j\omega)$ the transfer function.

$$h_r(t) = \int_{-\infty}^{t} \int_{-\infty}^{t'} h_i(t'')dt''dt' = IFT[H_r(j\omega)] = IFT\left[\frac{H(j\omega)}{(j\omega)^2}\right] \quad (1)$$

2.2. Profile Function

Herein, an incident direction to the target is given by an unit vector determined by its inclination angle θ and azimuthal angle ϕ in a spherical coordinate system (Figure 1). Therefore, we note an incident direction as $u(\theta, \phi)$. For example, the direction vector of axis x is represented by $x(90°, 0°)$.

First, we define the "geometrical" profile function of an object, in direction u, as its transverse cross sectional area, $A_g(u)$, along u. Figure 2 presents an example of geometrical profile function, $A_g(x)$, which is the area of transverse slices of the target at successive positions along the direction x.

The geometrical profile function is found to be approximately proportional to the transient ramp response of the target, $h_r(t)$ [5].

$$h_r(t) \approx -\frac{1}{\pi c^2} A_g(u) \quad \text{with} \quad u = \frac{ct}{2} \quad (2)$$

where c is the speed of light in freespace, t the time variable, and u the space variable.

With this property, for applications and experiments of ramp response imaging, the profile function of an arbitrary object, here

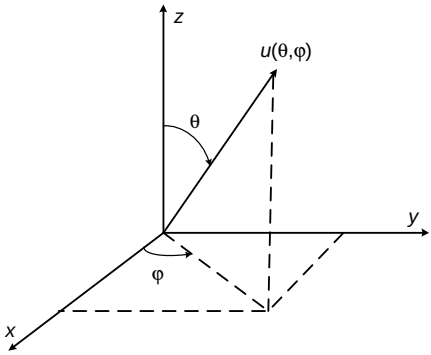

Figure 1. Definition of an unitary direction $u(\theta, \phi)$ in spherical coordinate system.

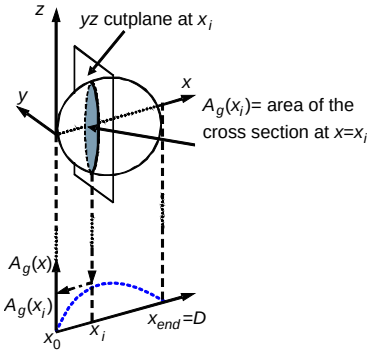

Figure 2. Illustration of the geometrical profile function of an object along x direction, $A_g(x)$. D is the characteristic dimension of the object in x direction.

defined as "physical" profile function $A_p(u)$, is obtained from its transient ramp response

$$h_r(t) = -\frac{1}{\pi c^2} A_p(u) \tag{3}$$

To make sure the physical profile function, A_p, is a valid estimate of the geometrical profile function, A_g, the frequency band determined by [5–7] should be matched to the upper Rayleigh and Resonance regions corresponding to the target's characteristic dimension.

$$f = [f_{\min}; f_{\max}] = \left[\frac{c}{200D}; \frac{2c}{D}\right] \tag{4}$$

The low frequency limit can be increased by extrapolation methods [21].

2.3. Image Reconstruction

Taking advantage of the ramp response technique, there are two reconstructions algorithms permitting to obtain approximate contours with no more than 3 observing directions. The initial reconstruction algorithm from profile functions proposed by Young, named "approximate limiting surface", uses a set of hyperbolic surfaces limiting the contour of the object for each of 3 observing directions [6, 7] and it is limited to single convex objects. On the contrary, the reconstruction algorithm presented in [17], highly reduces

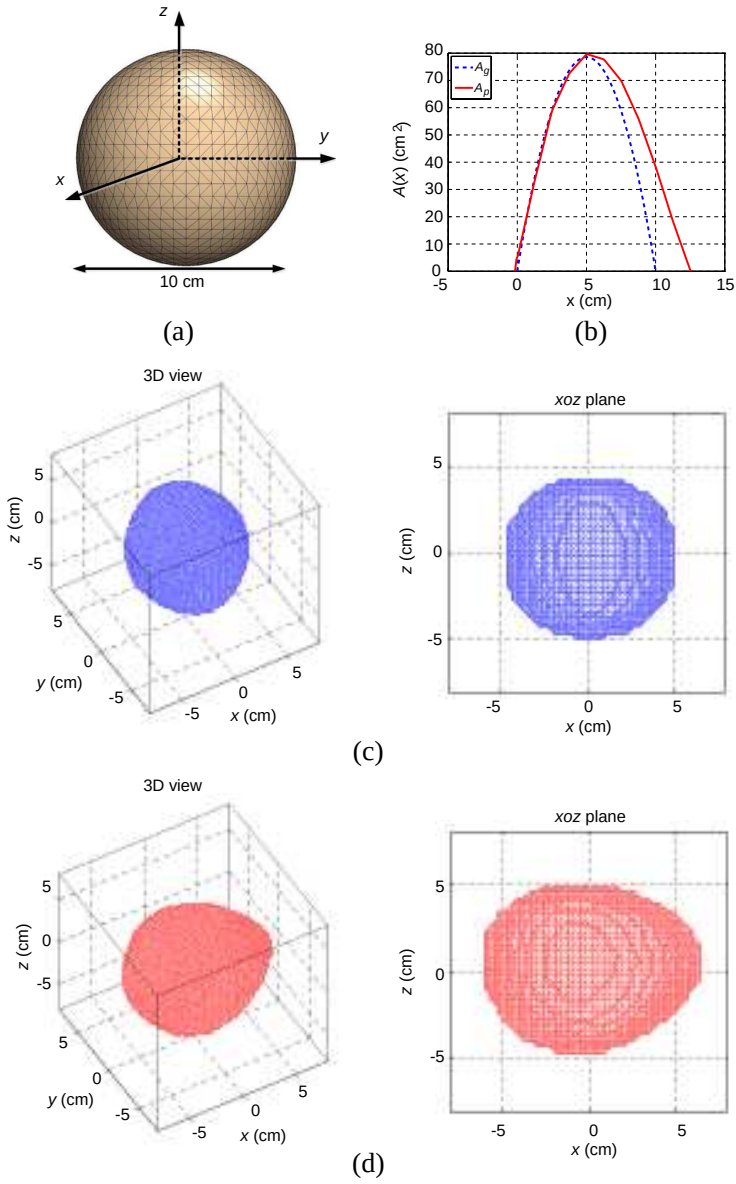

Figure 3. Configuration of study for a PEC sphere: (a) object shape ($D = 10\,\text{cm}$), (b) comparison between physical and geometrical profile functions. Reconstructed images from (c) geometrical and (d) physical profile functions, with scan direction x.

the bias of Young's algorithm, and therefore improves the accuracy of reconstructed objects. At each point, the product of profile functions from 3 observing directions, which is a weight function accounting for the probability that the point belongs to the object, is calculated. For each cut-plane along a given direction, those points with the highest values of the product are chosen such that the area of this slice is equal to its profile function.

To present the performance of image reconstruction from profile functions, we show two examples of PEC (Perfectly Electric Conducting) objects in freespace, taken from [17]: a sphere of diameter $D = 10\,\text{cm}$ (Figure 3) and an asymmetric object of length $D = 30\,\text{cm}$ (Figure 4). Both objects are illuminated by waves from 3 mutually orthogonal directions of observation (x, y, z), namely $x(90°, 0°)$, $y(90°, 90°)$ and $z(0°, 0°)$, respectively. Far-field transfer functions at chosen directions are obtained using an electromagnetic simulation software, FEKO [22], with the frequency band given by (4) equal to [15 MHz; 6 GHz] for the sphere of diameter $D = 10\,\text{cm}$, and [5 MHz; 2 GHz] for the asymmetric object of length $D = 30\,\text{cm}$, respectively. Then ramp responses and physical profile functions are calculated by (1) and (3). Note that we choose to center the target and its resulting profile functions at the origin of the Cartesian coordinate system (x, y, z).

Firstly, because of the symmetry properties of the sphere, we only present, in Figure 3(b), the comparison between the physical profile function, $A_p(x)$, and the geometrical one, $A_g(x)$, along x direction. Difference between them are mainly due to the shadow region effect [17]. We apply the algorithm in Section 2.3 to reconstruct 3D images from the two sets of profile functions with the same scan direction x. From the outcome, Figure 3(c) is visually in agreement with the initial sphere. While, due to the bias introduced by the shadow region effect, Figure 3(d) is slightly distorted.

Secondly, for the asymmetric object, geometrical and physical profile functions in directions (x, y, z) are compared in Figure 4(b). Once again, with orthogonal geometrical profile functions, a well-reconstructed 3D image (Figure 4(c)) is obtained by this reconstruction algorithm. On the contrary, due to the shadow region effect, physical profile functions result in a strongly distorted image, (Figure 4(d)).

This reconstruction algorithm manages to effectively exploit information to reconstruct non-convex object and multiple separated objects from only 3 profile functions and directly gives satisfactory estimates with orthogonal directions [17, 23, 24]. Its limitations mainly lie in two aspects: (a) Due to the shadow effect in physical profile functions, the distortion of reconstructed objects is significant,

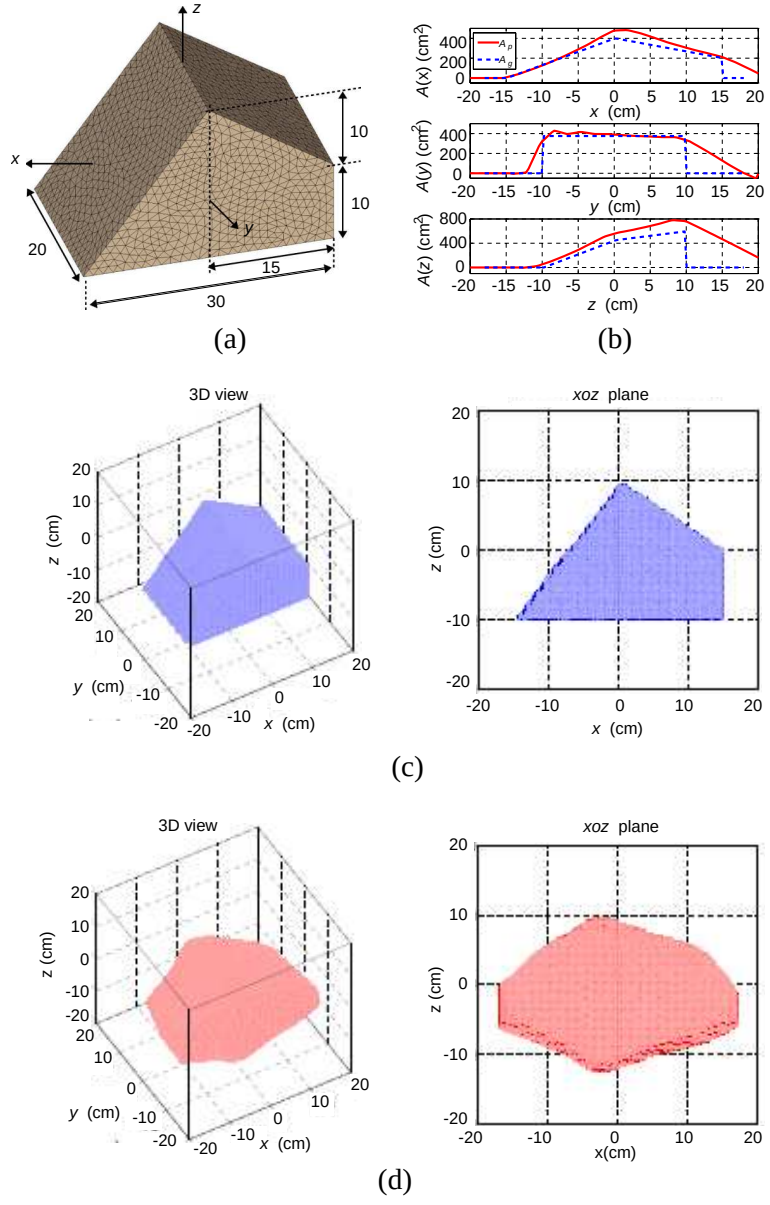

Figure 4. Configuration of study for a PEC asymmetric object: (a) object shape ($D = 30\,\text{cm}$), (b) comparison between physical and geometrical profile functions. Reconstructed images from (c) geometrical and (d) physical profile functions, with scan direction x.

especially for asymmetric or complicated objects. Therefore quality evaluation of reconstructed objects and further identification are required. (b) Poor performance for non-orthogonal directions [25]. This limitation can be overtaken by a further iterative fitting process with a priori information on the target and the addition of other view angles.

Therefore, to overcome the above limitations and to further identify objects from their reconstruction, we propose to calculate profile functions of 3D reconstructed objects in arbitrary directions. Indeed, the algorithm for reconstructing a 3D object from its profile functions is an "inverse problem", while calculating the profile functions of a 3D object is a "direct problem".

3. ALGORITHM FOR CALCULATING PROFILE FUNCTIONS FROM A 3D OBJECT

3.1. Algorithm Description

Given a binary 3D object $O(x, y, z)$ enclosed in a computational domain C_D, it is difficult, and often almost impossible, to obtain analytically its geometrical profile function when it has an irregular shape. Therefore, we need to calculate it numerically.

The algorithm is described with the following steps:

- Firstly, as shown in Figure 5(a), we cut the computational domain in successive slices perpendicular to the observing direction $u(\theta, \phi)$ with a thickness δu, where δu is the discrete step in the direction $u(\theta, \phi)$. Hence, the slice S_i at position $u = u_i$ (middle plane of S_i) is the region enclosed by the plane at $u_{il} = u_i - \delta u/2$, the plane at $u_{ih} = u_i + \delta u/2$ and the edges of the computational domain C_D. The numerical profile function $A_c(u_i)$ at position $u = u_i$ can be calculated by:

$$A_c(u_i) = V_{S_i}/\delta u \tag{5}$$

where V_{S_i} is the volume of the slice S_i.

- Secondly, the computational domain C_D is distributed into N^3 elementary cubic pixels $P(x, y, z)$, each with a volume δu^3, where N is the number of discrete samples in each direction. The computational domain is represented by 2 different kinds of pixels: pixels inside the object (solid points) and pixels outside the object (hollow points). For simplification, we present it in Figures 5(b)–(c) in a two-dimensional view.

$$O(x, y, z) = \begin{cases} 1 & \text{if } P(x, y, z) \text{ inside object} \\ 0 & \text{if } P(x, y, z) \text{ outside object} \end{cases} \tag{6}$$

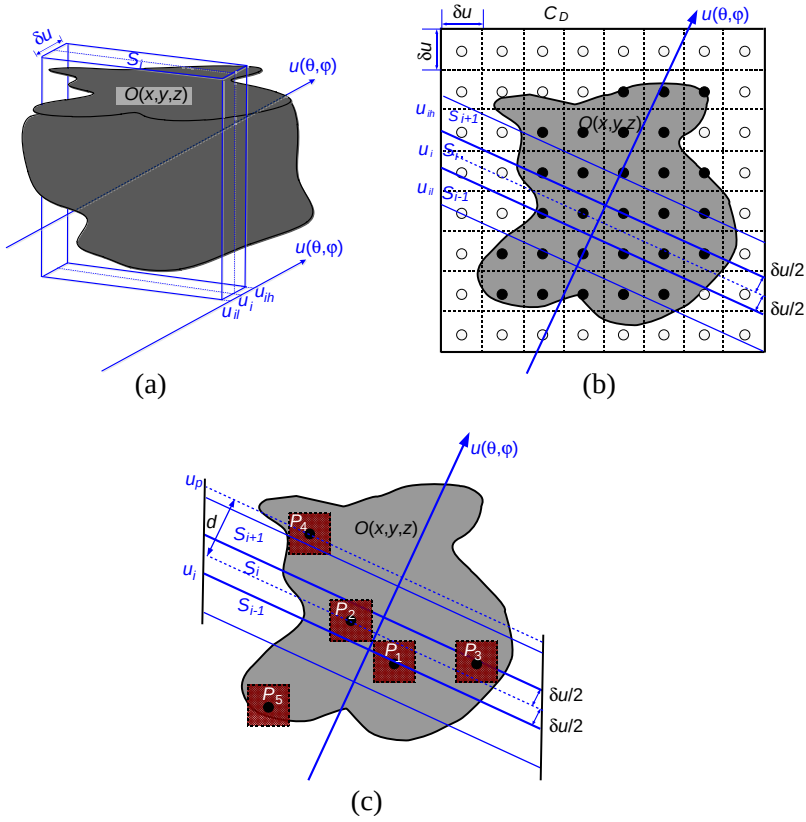

Figure 5. (a) Slices S_i in a three-dimensional view. (b) Slices S_i in a two-dimensional view. (c) Contribution of different types of pixels to the slice S_i.

- Thirdly, we set a weight function W to calculate the proportion that each pixel gives to slice S_i. Taking into account that points closer to u_i give higher contribution, we choose W as:

$$W = \begin{cases} 1 - |d/\delta u|; & d \in [-\delta u, \delta u] \\ 0; & \text{otherwise} \end{cases} \tag{7}$$

$d = u_P - u_i$ being the signed distance from the center of pixel P, with coordinate u_P along the direction vector u, to the plane at u_i.

According to the distance d, there are 5 different types of pixels P_1, P_2, P_3, P_4 and P_5, shown in Figure 5(c).

P_1: $-\delta u \leq d < 0$; it gives W to S_i and $1 - W$ to S_{i-1}.

P_2: $d = 0, W = 1$; it entirely belongs to S_i.

P_3: $0 < d \leq \delta u$; it gives W to S_i and $1 - W$ to S_{i+1}.

P_4: $d \geq \delta u$; its contribution for S_i is null.

P_5: $d \leq -\delta u$; its contribution for S_i is null.

- Fourthly, the volume of the slice S_i is obtained by summing up individual contributions from each pixel.

$$V_{S_i} = \sum_x \sum_y \sum_z W \times \delta u^3 \times O(x, y, z) \tag{8}$$

- Finally, combining (5) and (8), the numerical profile function $A_c(u_i)$ at position u_i is calculated by:

$$A_c(u_i) = \sum_x \sum_y \sum_z W \times \delta u^2 \times O(x, y, z) \tag{9}$$

3.2. Algorithm Verification

In order to quantitatively measure the difference between a reference profile function A_r and a profile function A_c computed by our algorithm, we define:

- the absolute error for slice S_i at position u_i along a given direction u as:

$$E(u_i) = |A_r(u_i) - A_c(u_i)| \tag{10}$$

- the relative global error for the given direction u as:

$$E_r(u) = \frac{\int E(u_i) du_i}{\int A_r(u_i) du_i} \tag{11}$$

To validate this algorithm, we consider two spheres (same configuration as Figure 3(a) in Section 2) with diameter $D = 10\,\text{cm}$ and $D = 30\,\text{cm}$, respectively. To completely enclose the studied objects, we choose a cubic computational domain of dimension $d_c = 45\,\text{cm}$, which is divided into $N^3 = 128^3$ pixels, with $\delta u = d_c/N = 0.35\,\text{cm}$. Note that, we use the same computational domain for all following tests in this paper.

For each sphere, we compare two types of profile functions:

- A_g^O, the known analytical geometrical profile function of the object, taken as the reference profile function for verification;
- A_c^O, the geometrical profile function computed by our algorithm from the object.

Because of the symmetry of the sphere, we only need to choose one direction $u(0°, 0°)$ to study the performance of this algorithm. Comparison between $A_g^O(u)$ and $A_c^O(u)$ for the two different spheres are shown in Figures 6(a) and (b) respectively, as well as their corresponding absolute errors for each slice. The relative global errors defined in (11) are 3% and 1% for the two spheres respectively. Figure 6(c) shows the effect of the discretization, with relative global errors $E_r(u)$ decreasing when the number of samples N increases. The larger sphere ($D = 30\,\text{cm}$) gives a lower relative global error since it is related to the object's dimension.

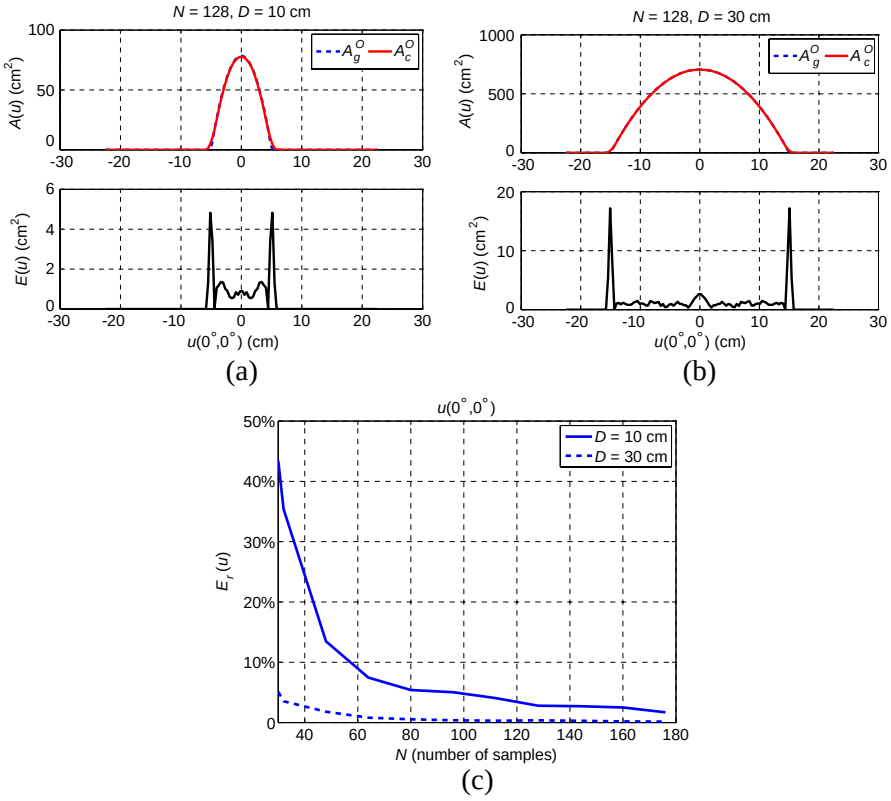

Figure 6. Comparison between the analytical geometrical profile function, $A_g^O(u)$, and the computed profile function, $A_c^O(u)$, at direction $u(0°, 0°)$ for the sphere with diameter (a) $D = 10\,\text{cm}$, (b) $D = 30\,\text{cm}$, (c) effect of the number of samples on the relative global error for the two spheres.

4. APPLICATIONS OF THE ALGORITHM OF PROFILE FUNCTION CALCULATION

In this section, we apply the algorithm of geometrical profile function calculation firstly to evaluate the quality of 3D image reconstruction from profile functions, and secondly to identify radar targets with a database of possible targets.

4.1. Quality Evaluation of 3D Image Reconstruction

Now, we apply our algorithm to evaluate the quality of 3D image reconstruction from profile functions, presented in Section 2. For simplification, we note:

- Rg, the 3D object reconstructed from analytical geometrical profile functions A_g^O, for example, the reconstructed sphere of Figure 3(c) or the reconstructed asymmetric object of Figure 4(c);
- Rp, the 3D object reconstructed from physical profile functions A_p^O, for example, the reconstructed sphere of Figure 3(d) or the reconstructed asymmetric object of Figure 4(d).

Correspondingly, we compute by our algorithm, presented in Section 3, the profile functions:

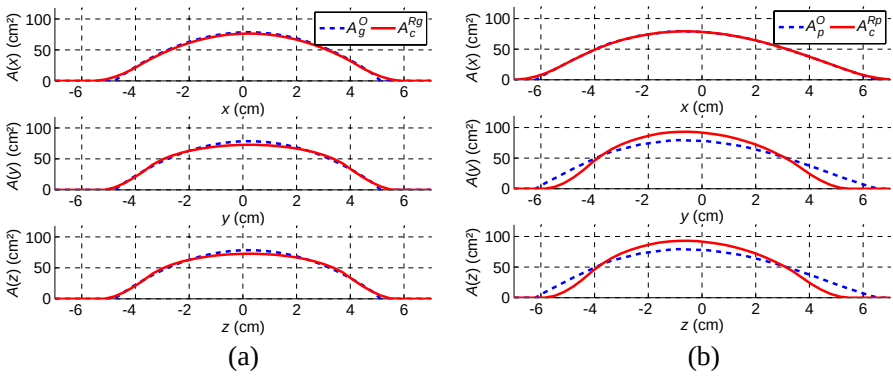

Figure 7. (a) Comparison between the analytical geometrical profile functions A_g^O of the initial sphere and the profile functions A_c^{Rg} computed from its reconstructed object Rg. (b) Comparison between the physical profile functions A_p^O of the initial sphere and the profile functions A_c^{Rp} computed from its reconstructed object Rp, in direction x, y, z, respectively.

- A_c^{Rg} from the 3D reconstructed object Rg;
- A_c^{Rp} from the 3D reconstructed object Rp.

The reconstruction algorithm uses profile functions at directions $x(90°, 0°)$, $y(90°, 90°)$ and $z(0°, 0°)$, we therefore consider the same directions.

Firstly, for the reconstructed sphere Rg, the analytical geometrical profile function A_g^O from the initial sphere is taken as the reference profile function. Comparison between A_g^O and A_c^{Rg} is shown in Figure 7(a). It shows quite small differences with relative errors 4%, 5%, 5% in directions x, y, z respectively, which confirms a very good agreement of the 3D reconstructed image with the initial sphere.

Secondly, for the distorted reconstructed sphere Rp, the physical profile function A_p^O from the initial sphere is taken as the reference profile function. Comparison between A_p^O and A_c^{Rp} is shown in Figure 7(b). The difference is more significant with relative errors equal to 1%, 21%, 21% in directions x, y, z respectively. The errors are higher for y and z, while it remains limited in x direction, because it is the scan direction of the reconstruction (Section 2).

Similarly, for the reconstructed asymmetric objects, comparison between initial profile functions (A_g^O or A_p^O) and the corresponding computed ones from the reconstruction (A_c^{Rg} or A_c^{Rp}) are presented in

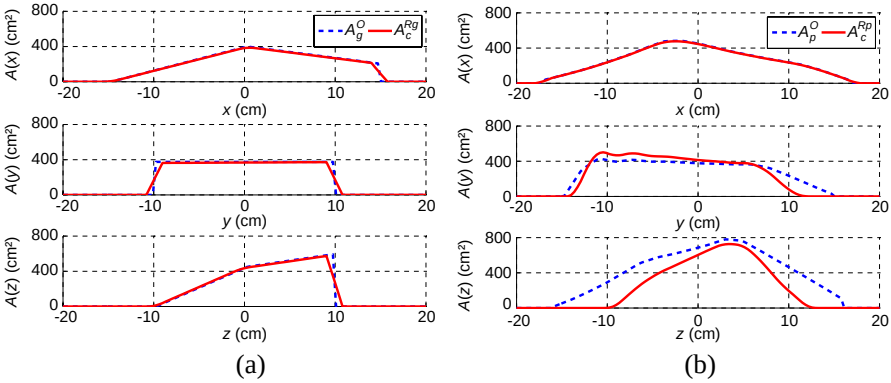

Figure 8. (a) Comparison between the analytical geometrical profile functions A_g^O of the initial object and the profile functions A_c^{Rg} computed from its reconstructed object Rg. (b) Comparison between the physical profile functions A_p^O of the initial object and the profile functions A_c^{Rp} computed from its reconstructed object Rp, in direction x, y, z, respectively.

Figures 8(a) and (b) respectively. Once again, the relative errors for the accurate reconstructed object *Rg* are smaller (3%, 6%, 6%) than the errors (2%, 21%, 37%) of the distorted reconstructed object *Rp* in directions x, y, z, respectively.

In conclusion, both examples demonstrate that the use of such computed profile functions is an efficient tool to quantitatively assess the quality the 3D image reconstruction from ramp responses and profile functions.

4.2. Identification of Radar Targets Using Profile Functions

To automatically identify a radar target, a common way consists in directly comparing its image to models in a database, for example the contour of the radar image and that of the models [20]. Here, we propose to use an alternative feature for the identification, the profile function along chosen directions, which can be calculated by the algorithm presented in Section 3. Before the identification process itself, we create a database containing K models of 3D objects.The method is given by following steps:

- Firstly, using the object's physical profile functions A_p^O in 3 directions, we obtain a 3D reconstructed object *Rp* by the image reconstruction algorithm presented in Section 2.
- Then, we choose L arbitrary directions. We note each direction $u^{(l)}$ as u in the following for simplification. By our algorithm for calculating profile functions presented in Section 3, we obtain the profile functions $A_c^{Rp}(u)$ computed from the reconstructed object *Rp* and the profile functions $A_c^M(u)$ computed from each model M.
- Next, for each direction u, using (10), we measure the absolute error $E(u_i)$, in each slice S_i at position u_i, between $A_c^{Rp}(u)$ and $A_c^M(u)$:

$$E(u_i) = \left|A_c^{Rp}(u_i) - A_c^M(u_i)\right| \tag{12}$$

From this error, $E(u_i)$, a function, $Sim(u_i)$, is defined to represent the similarity of slice S_i between the reconstructed object and each model:

$$Sim(u_i) = \begin{cases} 1 & E(u_i) \le E_{\min} \\ \frac{E_{\max} - E(u_i)}{E_{\max} - E_{\min}} & E_{\min} < E(u_i) < E_{\max} \\ 0 & E(u_i) \ge E_{\max} \end{cases} \tag{13}$$

where $E_{\min}$ and $E_{\max}$ are the minimum tolerance and maximum tolerance of error respectively.

For each slice, if the error $E(u_i)$ is adequately small, less than the minimum tolerance of error, we can consider that the slice at this position is totally matched. On the contrary, if this error is greater than the maximum tolerance of error, we consider it as unmatched.

Furthermore, we calculate the global similarity $Sim_g(u)$ of all slices along u as the similarity for this direction:

$$Sim_g(u) = \frac{\sum_{i=1}^{N} Sim(u_i)}{N} \tag{14}$$

where N is the number of slices along the direction u.

Finally, in this manner, the similarities of the L chosen directions give an overview similarity between the object and each model. Models with higher similarities are selected as the most possible shapes for the studied object.

Taking as studied object the Model 1 shown in Figure 9(a), we present the principle and performance of our method. For the database

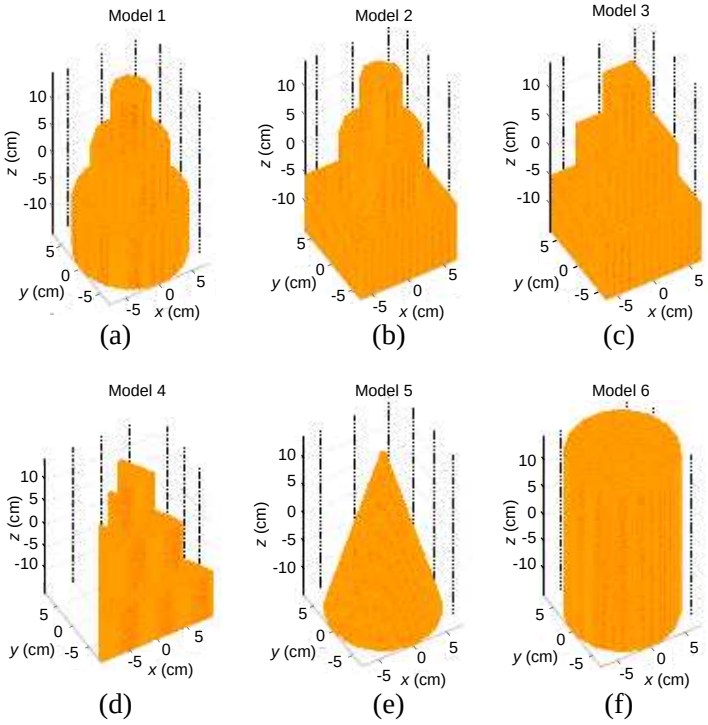

Figure 9. Configuration of 6 models: (a) Model 1, (b) Model 2, (c) Model 3, (d) Model 4, (e) Model 5, (f) Model 6.

of models, we only consider models which have same level of volume and similar shape as the studied object, because models of much larger or smaller dimension are not comparable. Hence, we consider $K = 6$ models shown in Figure 9: 4 step-cylinders, Model 1, 2, 3, 4, each with 3 sub-cylinders (circle, square or triangle cylinder), a cone (Model 5) and a circle cylinder (Model 6). For Models 1, 2, 3, 4, each slice in the same position along axis z has equal area, for example, at position z_i along axis z, the slice (a circle) of Model 1 and the slice (a square) of Model 3 have the same area. Each corresponding sub-cylinder of the 4 step-cylinders has equal height. Model 5 (the cone) and Model 6 (the circle cylinder) have the same diameter of the base and same height as the studied object, namely the Model 1. Detailed dimensions (in cm) of these models are presented in Table 1.

Table 1. Dimensions of the 6 models (in cm).

Model	Sub-cylinder	Diameter or side	Height
Step-cylinder	$Cylinder1$	5	10
	$Cylinder2$	10	10
	$Cylinder3$	15	10
Cone		15	30
circlecylinder		15	30

We use the same cubic computational domain of dimension 45 cm with $N^3 = 128^3$ pixels defined in Section 3. With the frequency band [5 MHz; 8 GHz], its ramp responses from 3 mutually orthogonal directions, $x(90°, 0°)$, $y(90°, 90°)$ and $z(0°, 0°)$, are obtained by FEKO [22]. The 3 physical profile functions A_p^O in the corresponding directions, calculated by (3), are shown in Figure 10(a). With the reconstruction algorithm in Section 2, we obtain a 3D reconstructed object shown in Figure 10(b). Applying our algorithm presented in Section 3, we can calculate the profile functions both for the reconstructed object and for each model, namely A_c^{Rp} and A_c^M in arbitrary directions. For each model, we calculate the similarity of each slice and the global similarity for each direction by (13) and (14), respectively. The choice of the minimum and maximum tolerances of error is somewhat arbitrary: it is related to the expected accuracy. With S_{C_D} the area of each slice of the computational domain, E/S_{C_D} is the ratio between the number of false pixels and the total number of pixels in each slice. Here, we choose $E_{\min}/S_{C_D} = 0.2$ and $E_{\max}/S_{C_D} = 6$.

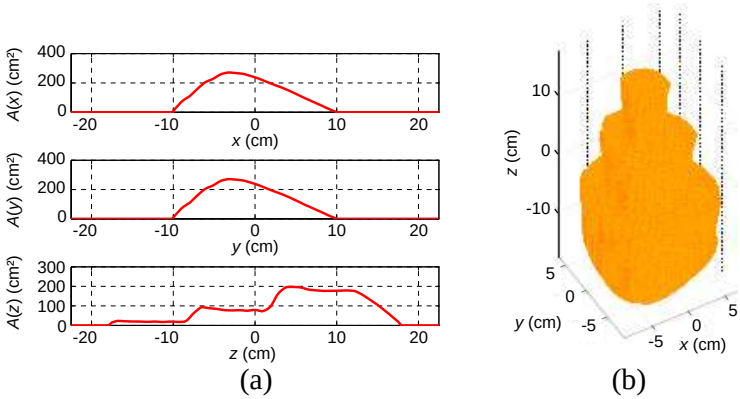

Figure 10. (a) Physical profile functions of the studied 'circle step-cylinder' in 3 mutually orthogonal directions $x(90°, 0°)$, $y(90°, 90°)$ and $z(0°, 0°)$. (b) Reconstructed image of the 'circle step-cylinder' obtained from the 3 physical profile functions, with scan direction z.

To show the performance of our method, we compare global similarities for the 6 models in some chosen directions. Firstly, we consider directions in xoz and yoz plane, namely directions with fixed azimuthal angle $\phi = 0°$ or $90°$ and inclination angle θ varying in $[0°, 180°]$ with a step $\delta\theta = 15°$. The global similarities between the object and the 6 models for the case $\phi = 0°$ and the case $\phi = 90°$ are presented in Figures 11(a) and (b) respectively. For each direction, the global similarities of Models 1, 2, 3 are very close, with slight differences among them. For $\phi = 0°$, Model 4, namely the triangle step-cylinder, has same level of global similarities as Model 1, 2, 3, while for $\phi = 90°$, it has much lower similarities so that we can separate it from the 3 other step-cylinders. Comparing to the 3 step-cylinders, Model 5 and 6 has lower similarities for most of the chosen directions. Secondly, we consider directions with fixed inclination angle, $\theta = 45°$ or $90°$, and azimuthal angle ϕ varying in $[0°, 180°]$ with a step $\delta\phi = 15°$. In the case of $\theta = 45°$, shown in Figure 11(c), we can classify the similarities of the 6 models into 3 levels: Models 1, 2, 3 have the highest similarities for all chosen directions; Model 4 has lower levels; Models 5 and 6 have the lowest levels for most of the directions. While in the case of $\theta = 90°$ shown in Figure 11(d), the difference between models is not significant, especially in the directions $\phi = [0°, 90°]$, but still, Models 1, 2, 3 have the highest similarities for most of the chosen directions.

To select the optimal model, we now calculate the mean of the global similarities $\overline{Sim_g}$ for the full range of possible directions, namely

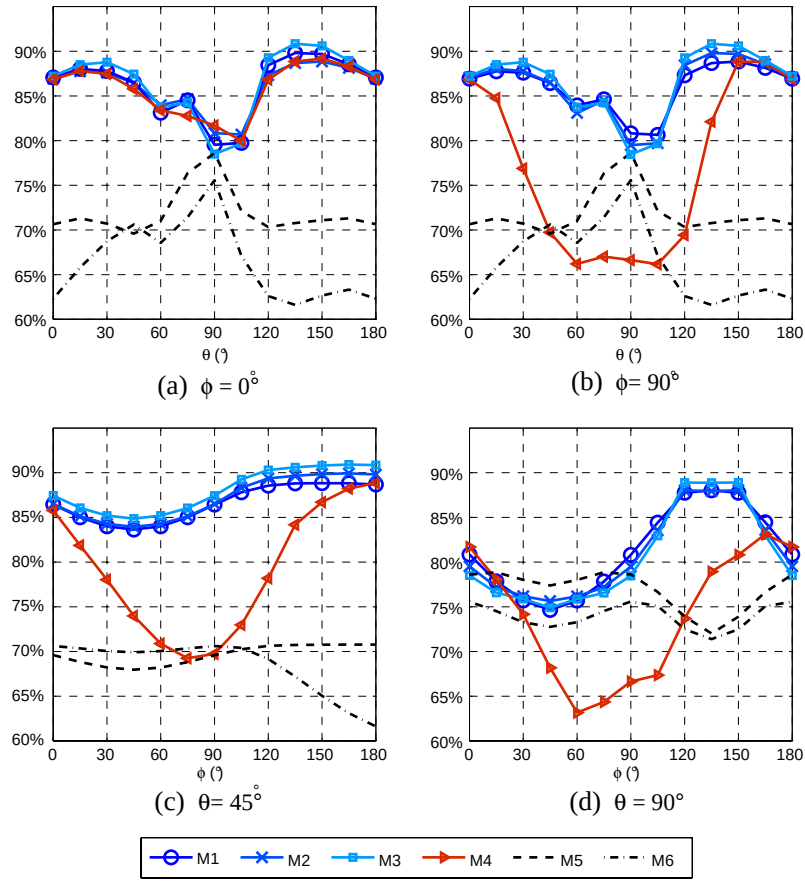

Figure 11. Global similarities $Sim_g(u)$ between the object and each model for chosen directions: (a) $\phi = 0°$, $\theta = [0°, 180°]$, (b) $\phi = 90°$, $\theta = [0°, 180°]$, (c) $\theta = 45°$, $\phi = [0°, 180°]$, (d) $\theta = 90°$, $\phi = [0°, 180°]$.

directions $u(\theta, \phi)$ with θ and ϕ both varying in [0°, 180°] with a step $\delta\theta = \delta\phi = 15°$. Table 2 gives the mean of the global similarities $\overline{Sim_g}$ for the whole set of directions for each model. From the outcome, the 3 'step-cylinders' (Models 1, 2, 3) have the highest mean similarity (around 86%) and cannot be distinguished. In fact, contrary to high frequency radar imaging, low frequency methods cannot give high resolution, i.e., details on the target, but they provide information only on the approximate shape of the target. Therefore, in our method, we have to consider that models 1, 2 and 3 are the same and we select them as the optimal models of the studied object.

Table 2. Mean of global similarities.

Model	Model 1	Model 2	Model 3	Model 4	Model 5	Model 6
$\overline{Sim_g}$	86%	86%	87%	82%	72%	66%

5. CONCLUSION AND PERSPECTIVES

In this paper, we have developed an algorithm for calculating profile functions from a 3D object. Firstly, it can be applied to quantitatively evaluate the quality of reconstructions by calculating errors between profile functions from the initial object and profile functions from its reconstructed image. Secondly, with a database containing possible models, it also can be applied to identify a radar target using its reconstructed object obtained from physical profile functions in only 3 directions. Our method permits to compare the reconstructed object and models in a full range of directions so as to avoid that different shapes might have same profile functions in some directions. Taking into account the poor condition of limited resolution encountered in low frequency radar imaging, we successfully find the best possible models for the studied object.

Existing reconstruction algorithms give distorted results for non-orthogonal directions, while in practice, radar equipments have a limited viewing angle for remote sensing or large targets. Therefore, an optimization process is required. Errors between profile functions of the initial object and profile functions of its reconstructed image are acknowledged as quantitative indicators for iterative fittings. Our future work aims to use the algorithm for calculating profile functions in arbitrary directions so as to get satisfactory reconstructions in the non-orthogonal case.

REFERENCES

1. Lynch, Jr., D., *Introduction to RF Stealth,* SciTech Publishing, 2004.
2. Moffatt, D. L., J. D. Young, A. A. Ksienski, H.-C. Lin, and C. M. Rhoads, "Transient response characteristics in identification and imaging," *IEEE Trans. Ant. Prop.*, Vol. 29, 192–204, Mar. 1981.
3. Kuschel, H., "VHF/UHF radar. Part 1: Characteristics," *Electronics & Communication Engineering Journal*, Vol. 14, No. 2, 61–72, Apr. 2002.

4. Kuschel, H., J. Heckenbach, S. Mller, and R. Appel, "Countering stealth with passive, multi-static, low frequency radars," *IEEE Aerospace and Electronic Systems Magazine*, Vol. 25, No. 9, 11–17, Sep. 2010.
5. Kennaugh, E. M. and D. L. Moffatt, "Transient and impulse response approximations," *Proceedings of the IEEE*, Vol. 53, 893–901, 1965.
6. Young, J. D., "Radar Imaging from ramp response signatures," *IEEE Trans. Ant. Prop.*, Vol. 24, 276–282, May 1976.
7. Young, J. D., "Target imaging from multiple frequency radar returns," Ph.D. Dissertation, The Ohio State University, Columbus, Jun. 1971.
8. Nag, S., "Ramp response signatures of dielectric scatterers," Ph.D. Dissertation, The Ohio State University, Columbus, Dec. 1971.
9. Shubert, K. A., J. D. Young, and D. L. Moffatt, "Synthetic radar imagery," *IEEE Trans. Ant. Prop.*, Vol. 25, 477–483, Jul. 1977.
10. Tsao, S.-J. J., "Image reconstruction using ramp response signatures," Ph.D. Dissertation, The Pennsylvania State University, May 1985.
11. Nag, S. and L. Peters, Jr., "Ramp response signatures of dielectric targets, especially land mines," *Geoscience and Remote Sensing Symposium Proceedings*, Vol. 1, 213–315, Jul. 1998.
12. Chen, C.-C. and L. Peters, Jr., "Ramp response signatures for UXOs," *Geoscience and Remote Sensing Symposium Proceedings*, Vol. 4, 1436–1438, 2000.
13. Nag, S. and L. Peters, Jr., "Radar radar images of penetrable targets generated from ramp profile functions," *IEEE Trans. Ant. Prop.*, Vol. 49, 32–40, Jan. 2001.
14. Chen, C.-C. and L. Peters, Jr., "Radar scattering and target imaging obtained using ramp-response techniques," *Antennas and Propagation Magazine*, Vol. 49, No. 3, Jun. 13–27, 2007.
15. Zhang, X. M., W. Lib, and G. R. Liu, "A new technique in ramp response for acoustic imaging of underwater objects," *Applied Acoustics*, Vol. 63, 453–465, 2002.
16. Li, W., G. R. Liu, and V. K. Varadan, "Acoustical imaging of underwater objects using the bistatic ramp response signals," *IOP, Smart Mater. Struct.*, Vol. 13, 169–174, 2004.
17. Chauveau, J. and N. de Beaucoudrey, "A new algorithm of 3D image reconstruction of radar targets from ramp responses in low frequency," *Progress In Electromagnetic Research M*, Vol. 16, 1–18, 2011.

18. Das, Y. and W. Boerner, "On radar target shape estimation using algorithms for reconstruction from projections," *IEEE Trans. Ant. Prop.*, Vol. 26, No. 2, 274–279, Mar. 1978.
19. Nebabin, N. G., *Methods and Techniques of Radar Recognition,* Artech House, London, 1994.
20. Anton, L. and S. Pican, "Reconstruction and recognition of the radar target image," *5th International Conference on Telecommunications in Modern Satellite, Cable and Broadcasting Service, TELSIKS 2001*, Vol. 1, 61–64, 2001.
21. Chauveau, J., N. de Beaucoudrey, and J. Saillard, "Radar target imaging from ramp responses using low frequency extrapolation," *Progress In Electromagnetics Research Symposium Abstracts*, 18–21, Moscow, Russia, Aug. 18–21, 2009.
22. FEKO, Software of Electromagnetic Simulations, http://www.feko.info.
23. Chauveau, J., N. de Beaucoudrey, and J. Saillard, "Low frequency radar targets 3-dimensional imaging using ramp response signatures," *International Radar Conference*, Bordeaux, France, Oct. 12–16, 2009.
24. Chauveau, J. and N. de Beaucoudrey, "Low frequency imaging of separated objects using the ramp response technique," *IEEE International Symposium on Antennas and Propagation and CNC/USNC/URSI Radio Science Meeting*, Toronto, Ontario, Canada, Jul. 11–17, 2010.
25. Chauveau, J., Y. Wen, and N. de Beaucoudrey, "Low frequency radar target imaging using ramp response signatures in arbitrary directions," *PIERS Proceedings*, 1572–1575, Marrakesh, Morocco, Mar. 20–23, 2011.